

Plasma Spraying of Solution Precursor in Pulsed Mode: In-Flight Phenomena and Coating Deposition

F. Mavier¹ · F. Zoubian¹ · M. Bienia¹ · J. F. Coudert¹ · M. Lejeune¹ · V. Rat¹ · P. André²

Received: 27 October 2017 / Accepted: 23 February 2018 / Published online: 5 March 2018
© Springer Science+Business Media, LLC, part of Springer Nature 2018

Abstract In the field of plasma spray technologies, new processes were developed in order to obtain coatings with nanostructured architectures. Among them, solution precursor plasma spraying is a promising technique. However, to be industrially viable, efforts must be made to understand and control the steps of the process. In alternative to instabilities attenuations, the time-modulation of current–voltage characteristics of a low-powered arc plasma jet was proposed, resulting in time-modulation of plasma properties. This modulation was synchronized with a drop-on-demand printhead for injection to improve the control of plasma/material interaction. An aluminum nitrate ink was formulated to be compatible with a drop-on-demand printhead dispenser. Plasma composition was calculated by the Gibbs free energy minimization method. Moreover, in-flight diagnostics coupled with coating characterization were carried out. Results showed that the controlled injection system leads to the formation of vapors of aluminum oxide that led to the deposition of nanostructured cauliflowers-like structures. Amorphous alumina coatings with inclusions of γ -alumina micro-sized particles were obtained and a description of main in-flight mechanisms was proposed.

Keywords Solution precursor plasma spraying (SPPS) · Aluminum nitrate · Ceramic coatings · Ink-jet printing · Plasma chemical composition · Diagnostics · Arc instabilities

✉ V. Rat
vincent.rat@unilim.fr

¹ CNRS, IRCER, UMR 7315, University of Limoges, 87000 Limoges, France

² CNRS, LPC, UMR6533, University of Clermont Auvergne, 63000 Clermont-Ferrand, France

Introduction

Atmospheric arc plasma spraying is a well-established deposition method and allows elaborating metallic and ceramic coatings for various industries. The increasing use of thermal spray coatings in many end-use industries, such as aerospace, automotive, healthcare, energy and power, electronics, and agriculture, among others, is expected to fuel the growth of the thermal spray coatings market in the coming years. Versatility, absence of post-treatment, high efficiency and the possibility of deposition at atmospheric pressure are the mainly advantages of plasma spraying [1–3]. However, conventional plasma spraying does not allow nanostructured architectures for these applications so that new techniques have been developed in the last 10 years. Among the different ways explored, the most promising is plasma spraying of liquid feedstock such as Suspension Plasma Spraying (SPS) or Solution Precursor Plasma Spraying (SPPS).

In the latter, a liquid phase composed of solvent containing dissolved salts is injected within a thermal plasma jet as a liquid jet or a droplets spray. After the solvent evaporation, the precursors precipitate in-flight and the resulting materials interact with the plasma to form a nanostructured deposit on the substrate [4–10]. SPPS is simpler than SPS to formulate (no particles agglomeration and sedimentation in liquid phase) and exhibits good homogeneity of the dissolved materials provided the solubility threshold is not reached.

However, the solution injection makes the SPPS process approach more complex. It indeed requires considering the fragmentation of the liquid, the control of vaporization, the nature of the precipitation reactions of the dissolved salts and the chemical transformation of the precursor which leads to the final coating. A poor thermal treatment of the droplet can lead to the formation of a characteristic dried residue on the substrate. The concentration of the solution plays a key role in precipitation, leading to the formation of aggregates, dense particles or shells depending on its value [11].

Solution precursor treatment depends on plasma properties generated by a Direct Current (DC) arc plasma torch and the injection method. Difficulties in liquid spraying originate from:

- The dynamics of the electric arc: the electric arc motion leads to a temporal fluctuation of power and enthalpy [12, 13].
- The turbulence flow of the extinguishing jet which is characterized by short jet length, non-uniform radial temperature distribution and high axial temperature [14–16].
- The injection of the liquid material: continuous injection results in different fragmentation regimes that are difficult to control [17].

New torch designs (cascaded arc) are used to limit the amplitude of the arc root motion [18] and they are associated with mechanical or atomization injection systems which produce continuous liquid jet. Recently, an alternative approach has been proposed that relies on the amplification of arc electric instabilities to form a pulsed arc jet [19–24]. The basic idea is to modulate plasma properties and to synchronize the liquid injection with a drop-on-demand printhead to control the moment of liquid injection in order to improve the material treatment.

The objective of this paper is to describe the decomposition of a solution precursor containing aluminum nitrate to deposit finely structured alumina coatings by means of atmospheric plasma spraying of liquid feedstock in pulsed mode. In the following, we first describe the experimental setup. Secondly, the plasma chemical composition with an aluminum nitrate precursor solution is calculated by using the minimization of the Gibbs free energy at thermal and non-thermal equilibrium conditions and also considering liquid

and solid phases. Third, in-flight diagnostic results are presented as well as some coating properties. Lastly, a scenario for the mechanisms of precursor decomposition leading to these coatings is discussed.

Experimental Setup

The Pulsed Arc Plasma Torch

Previous studies have shown that the coupling of the Helmholtz and restrike modes in DC arc plasma torches can lead to a resonance mode called “Mosquito mode” [19–25] which generates a self-sustained pulsed arc jet with periodic arc voltage oscillations around 1.4 kHz at atmospheric pressure. Recent works have proved that the stability of this mode is improved by the modulation of the arc current [25]. The arc motion is influenced by the arc current modulation because the controlled variation of the arc radius affects the arc reattachment through the cold boundary layer upstream and favors the restrike mode. This allows extending the pulsed mode for durations compatible with deposition conditions. A power supply (Micronics systems, France) was used to impose a sinusoidal waveform to the current. This current modulation was optimized for 1.4 kHz modulation, the mean arc current is 25 A with a peak-to-peak current amplitude of 11.3 A. (see Fig. 1a) [25]. An example of the arc voltage signal is given in Fig. 1b. Voltage signal displays a typical saw-tooth shape and changes between 30 and 85 V. The electrical power, illustrated in Fig. 1c, is significantly modulated between 750 and 2200 W and its mean value is about 1500 W.

The operating parameters are summarized in Table 1. The torch operated at atmospheric pressure. The plasma forming gas was pure nitrogen (99.999% Alphagaz1, Air liquid), the anode diameter was 4 mm and the average specific enthalpy, estimated by measuring thermal losses, was about 17 MJ kg^{-1} .

The pulsed mode, also assimilated to a “controlled restrike”, strongly impacts the plasma jet behavior. Time resolved-imaging highlighted the structure of the extinguishing jet (Fig. 2). After restrike (just after trigger t_1 in Fig. 1, i.e. after the arc reattachment upstream in the nozzle), the nozzle discharges its remaining plasma gas. Then, a ball of plasma is emitted corresponding to plasma regions containing high enthalpy (Fig. 2, trigger t_2). The upstream arc then progresses and generates a new plasma ball identical to the previous one (Fig. 2, triggers t_3 and t_4). The plasma is structured in a pulsed jet at the same frequency as the electrical power. A long laminar pulsed jet is produced with 60–80 mm in length as illustrated in Fig. 3, due to the decrease of turbulence.

The Drop-on-Demand Dispenser and Ink Formulation

The injection system was a drop-on-demand printhead (MJ-ATP-01, Microfab, USA) corresponding to a glass capillary with a $80 \mu\text{m}$ aperture. The ejection is actuated by a piezoelectric crystal generating an individual droplet for each pulse trigger.

Aluminum nitrate was first chosen for its very good solubility in water (maximum of 69 g per 100 mL of water) permitting a significant material injection rate. Secondly, it was reported to thermally decompose to form aluminum oxides [8, 26, 27].

The aluminum nitrate nonahydrate ($\text{Al}(\text{NO}_3)_3 \cdot 9\text{H}_2\text{O}$, 98%, Alfa Aesar, Germany) salt was dissolved into deionized water. To fit the viscosity and surface tension requirements

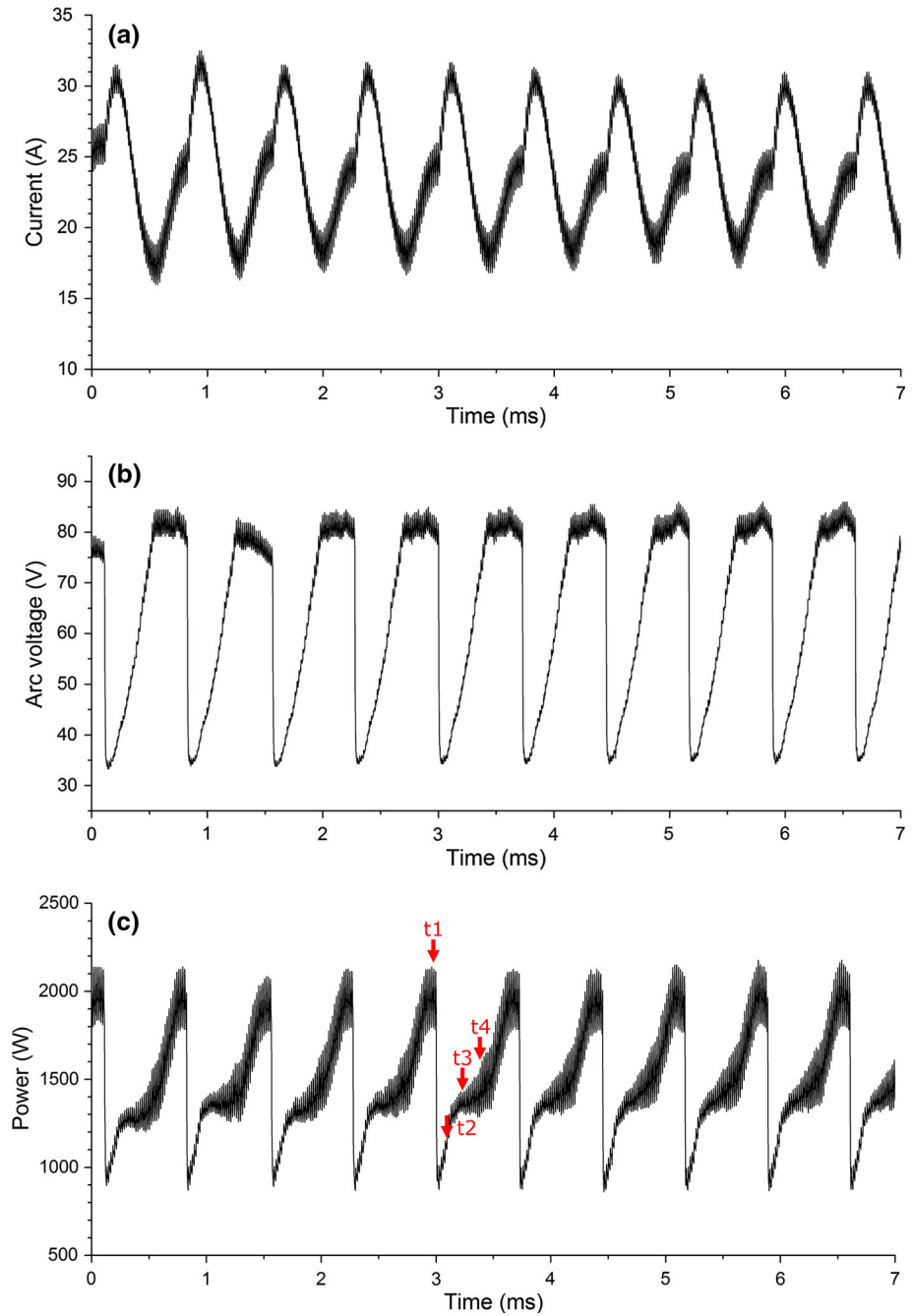


Fig. 1 Current (a), voltage signal (b) and power (c) of a pulsed arc plasma mode. (Triggers t_1 , t_2 , t_3 and t_4 are related to Fig. 2) (Color figure online)

Table 1 Torch operating parameters

Parameter	Value
Average current	25 A
Current modulation	$f = 1400 \text{ Hz}; \frac{\Delta I}{I} = 0.45$
Average enthalpy	17 MJ kg^{-1}
Average power	1.5 kW
Anode nozzle diameter	4 mm
Plasma gas	Nitrogen
Gas flow rate	2 slm

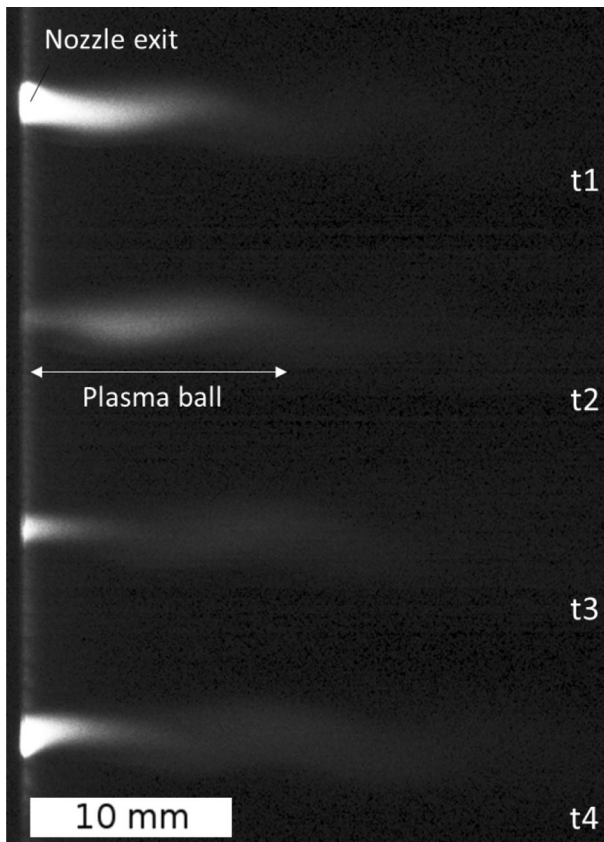
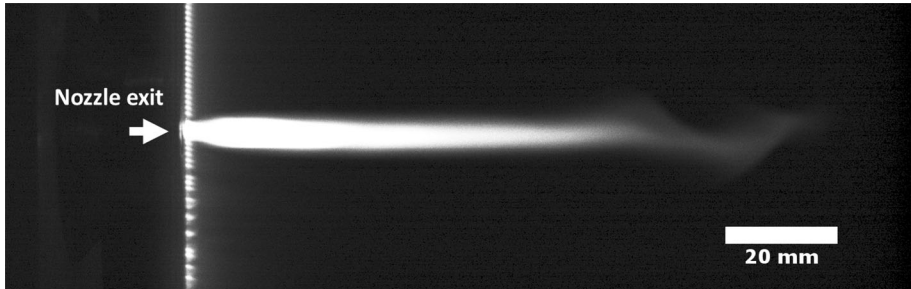


Fig. 2 Pulsed plasma jet. Synchronous imaging at different triggers (t1 to t4), see the red arrows on the power signal of Fig. 1c. Aperture time: 50 μs

given by the printhead manufacturer, glycerol (Extra pure 99 + %, Alfa Aesar, Germany) was added to increase the viscosity of the initial solution (from 1.7 to 7 mPa s) and a surfactant (BRIJ58, Polyethylene glycol hexadecyl ether, $\text{HO}(\text{CH}_2\text{CH}_2\text{O})_{20}\text{C}_{16}\text{H}_{33}$, Sigma-Aldrich, USA) was added to decrease the surface tension (from 76.5 to 41.4 mN m^{-1}).

Table 2 Mass percentages of the optimized aluminum ink

Compound	Mass %
Aluminum nitrate nonahydrate	30
Water	46
Glycerol	23
Ammonia	0.7
Surfactant	0.3

**Fig. 3** Pulsed plasma jet imaging. Aperture time: 500 μ s

The ejection ratio Z must be adapted to obtain a proper injection with no satellite droplets. This ratio involves Reynolds (Re) and Weber (We) numbers. It must be between 1 and 10 for correct ink jet ejection [28]. It is defined by Eq. 1 and optimized at $Z = 6.3$.

$$Z = \frac{Re}{\sqrt{We}} = \frac{\sqrt{\rho\gamma r}}{\eta} \quad (1)$$

where ρ is the droplet density, γ the surface tension, r the radius of the droplet, η the dynamic viscosity of the ink.

At last, a small quantity of ammonia was added to increase the pH (from 1 to 2) to satisfy the manufacturer requirements. The mass composition of the optimized solution is reported in Table 2.

Ejection test (without plasma) were performed to estimate the speed and the quality of the ejection. The actuation electrical pulse applied to the piezoelectric crystal was adjusted to avoid satellite droplets or in-flight fragmentation.

By comparison with the continuous injection (atomization or mechanical injection), the Drop-On-Demand (DOD) printhead allows controlling the quantity and the timing of the liquid injection with respect to the fluctuations of the plasma properties. The volume flow rate of the ink was $180 \mu\text{L min}^{-1}$ and the droplets velocity at the exit of the dispenser was $3.2 \pm 0.1 \text{ m s}^{-1}$.

Ink Thermal Characteristics

Under nitrogen atmosphere, Melnikov et al. reported a mechanism of thermal decomposition of aluminum nitrate octahydrate which involved the formation of amorphous aluminum oxide and the emission of nitric acid, nitrogen oxide and oxygen [27]. Pacewska and Keshr [26] highlighted the successive steps of dehydration of the aluminum nitrate

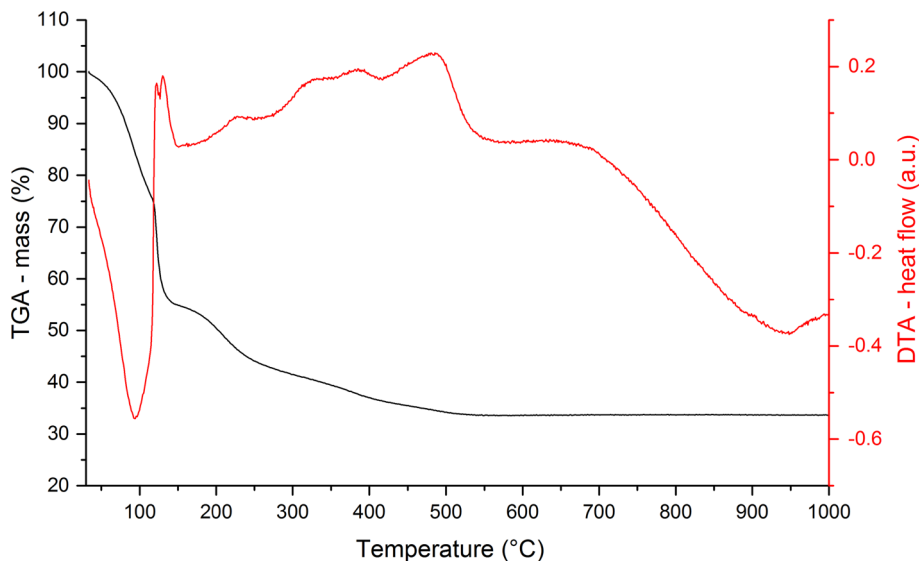


Fig. 4 Thermogravimetry analysis (left axis) and differential thermal analysis (right axis) of optimized nitrate aluminum ink

under air atmosphere and showed that the samples had remained amorphous up to 1000 °C but with a substantial temperature dependence of their porosity. The chemical transformations were reported to be all endothermic in [26, 27]. However, Shivakumar et al. [8] reported the crystallization of alumina oxide around 900 °C under oxygen. Moreover, the role of organic solvents, such as acetic acid, when spraying aluminum acetate, was shown to contribute to release combustion heat during their decomposition [8].

Consequently, the use of glycerol in aluminum nitrate ink can lead to exothermic reactions either because of oxygen from the thermal decomposition of the ink or from the air mixing during spraying.

Differential thermal analysis (DTA) and thermogravimetry analysis (TGA) were therefore carried out (TG-DSC Labsys evo, Setaram Instrumentation, France) under air atmosphere.

TGA gives the mass losses whereas DTA follows the temperature difference between sample and an inert reference to highlight exothermic and endothermic reactions. They allowed characterizing the evaporation of the solvent and the decomposition of the precursors in the solution. The samples (10.5 mg) were heated in an alumina crucible at a rate of 10 °C min⁻¹ from 20 to 1000 °C.

TGA/DTA results are shown in Fig. 4. Between 60 and 120 °C, the mass loss (30%) is attributed to water removal as also confirmed by the DTA endothermic reaction. Between 120 and 150 °C, an exothermic reaction is detected with a mass loss of about 15%. At last, between 150 and 500 °C, the mass loss is progressive with shoulders exhibiting exothermic reactions. The decomposition is complete around 500 °C, at least up to 1000 °C, as also shown in [26, 27]. It is worth mentioning that no crystallization process is observed below 1000 °C. According to the supplier's data, the nitrate salt is gradually decomposed from 135 °C. Moreover, the initial temperature of mass loss of glycerol depends on purity, water mass percentage and heating rate (10% mass loss at about 140 °C, 20% mass loss at about 177 °C) [29].

Overlaying reactions including dehydration and heat release from combustion of carbonaceous precursors can be expected like in the case of the use acetate aluminum as solution precursor [8]. The abrupt mass loss between 120 and 150 °C suggests a rapid combustion process which is probably different from that observed between 150 and 500 °C. It is interesting to note that the glycerol pyrolysis leads to the formation of methane (CH₄) and syngas (H₂ + CO) which the combustion could be responsible for exothermic reactions [30].

In order to gain a deeper insight into the temperature dependence of species formed after solution decomposition, thermodynamic calculations of chemical composition were performed.

Calculation of Plasma Chemical Composition Method

The decomposition of droplet as a function of temperature was estimated by calculating the thermodynamic chemical composition up to 9000 K. The first calculation considered the droplet alone regardless the surrounding atmosphere. This approach permitted to focus on the species formed due to the solution thermal decomposition following data given by Table 2. The second calculation took into account pure nitrogen as plasma forming gas. In the latter case, the composition of the plasma was, in molar percentages, 98.921% of nitrogen (N₂), 0.978% of water (H₂O), 0.0238% of aluminum nitrate (Al(NO₃)₃) and 0.0753% of glycerol (C₃H₈O₃). Note that the water molar percentage contains the water contribution of the aluminum nitrate nonahydrate. Ammonia for ink pH adjustment and surfactant were neglected due to their very low content in the ink. However, the formation of NH₃ was allowed by the thermodynamic calculations. The comparison between both calculations allowed highlighting the influence of nitrogen on droplet decomposition.

In the calculation, it was taken into account alumina Al₂O₃ in solid phase, aluminum oxide in liquid phase, aluminum nitride in solid phase and aluminum in solid and liquid phases. The various phases of alumina (α , δ , γ ...) were not distinguished. The liquid was considered to be an ideal liquid and Van der Waals interactions were neglected. At last, the condensed phases were immiscible.

Seventeen monatomic species were taken into account: Al, Al⁻, Al⁺, Al⁺⁺, C, C⁻, C⁺, H, H⁺, H⁻, N, N⁺, N⁺⁺, O, O⁻, O⁺ and O⁺⁺.

36 diatomic species Al₂, AlH, AlN, AlO, AlO⁺, C₂, C₂⁻, C₂⁺, CH, CH⁻, CH⁺, CN, CN⁻, CN⁺, CO, CO⁻, CO⁺, H₂, H₂⁻, H₂⁺, N₂, N₂⁻, N₂⁺, NH, NH⁻, NH⁺, NO, NO⁻, NO⁺, O₂, O₂⁻, O₂⁺, OH, OH⁻, OH⁺.

76 polyatomic species Al₂O, Al₂O₂, Al₂O₂⁺, Al₂O⁺, AlO₂, AlO₂⁻, AlHO(hydride), AlHO(hydroxyde), AlHO₂, AlHO⁻, AlHO⁺, AlO₂⁻, AlO₂, C₂H, C₂H₂, C₂H₄, C₂H₄O, C₂N, C₂N₂, C₂O, C₃, C₃O₂, C₄, C₄N₂, C₅, CH₂, CH₂O, C₂H₃, C₂H₅, C₂H₆, COOH, HCOOH, CH₃O, CH₂OH, CH₃OH, C₂H₅OH, HCCN, CH₃, CH₄, CHN, CHNO, CHO, CHO⁺, CNN, CNO, CO₂, CO₂⁻, CO₂⁺, H₂N, H₂N₂, H₂O, H₃N, H₃O⁺, H₄N₂, HNO, HNO₂(cys), HNO₂(trans), HNO₃, HO₂, H₃⁺, HO₂⁻, H₂O⁺, H₂O₂, N₂O, N₂O₃, N₂O₄, N₂O₅, N₂O⁺, N₃, NCN, NO₂, NO₂⁻, NO₃, NO₃⁻, NH₄⁺, NH₂OH, NH₂NO₂, O₃ and electrons.

Minimization of the Gibbs free energy at equilibrium and out of thermal equilibrium was used to calculate the plasma composition. Non-equilibrium conditions could be expected due to the liquid phase injected in hot plasma jet. The mean energy available inside the plasma, $\bar{E}_p = \dot{m}_p/h_p/f_0$ where \dot{m}_p , h_p and f_0 are respectively the gas mass flow rate, the mean enthalpy and the plasma frequency, is much higher than the energy needed to

vaporize the droplet $\bar{E}_d \approx \dot{m}_\ell L_v / f_i$ where \dot{m}_ℓ , L_v and f_i are respectively the mass flow rate of liquid, the latent heat of vaporization and the frequency of injection ($f_i = f_0$, $\bar{E}_p \approx 0.2 \text{ J}$ and $\bar{E}_d \approx 0.004 \text{ J}$). Consequently, when injecting liquid, moderate thermal non-equilibrium ($\theta = T_e / T_h = 2$) was supposed.

Details and assumptions about the calculation method and the internal temperatures are given in Ref. [31].

In-Flight Diagnostics

In-flight interactions of liquid with plasma were recorded by a fast-shutter CCD camera (Pixelfly, PCO, Germany), coupled with a 50 W laser diode (HiWatch, Oseir, Tampere, Finland) to illuminate the droplets at the emission wavelength of 801 nm. The fast-shutter camera and the laser were triggered by the synchronization system. A camera (Nikon D700, Japan) was used for imaging.

Optical emission spectroscopy (OES) was used to investigate the plasma radiation emission. Analyses were performed with an Isoplan spectrometer from Princeton Instruments (Trenton, NJ, USA). The focal length was equal to 320 mm and the focal plane size was 27 mm wide and 14 mm high. The spectrograph was associated with a high resolution intensified CCD camera (PIMAX4 1024i, Princeton Instruments, USA). A tungsten ribbon lamp, power-supplied by a current-regulated source, was used to calibrate the spectral intensities. A pyrometer was used to measure the tungsten ribbon temperature at a given lamp current. The spectral radiance of the tungsten ribbon lamp was calculated for a given temperature using Planck's law and the spectral emissivity of tungsten is given by De Vos [32]. The system was controlled by the software Lightfield (Princeton instruments, Trenton, USA) which allows the acquisition and the post processing of the emission spectra. The acquisition time was equal to 28 ms for 20 accumulations permitting the increase of the signal to noise ratio. This corresponds to temperature measurements averaged over about 40 periods of arc voltage. Measurement of plasma temperature was carried out with Specair software which simulates emission spectra of air plasma [33].

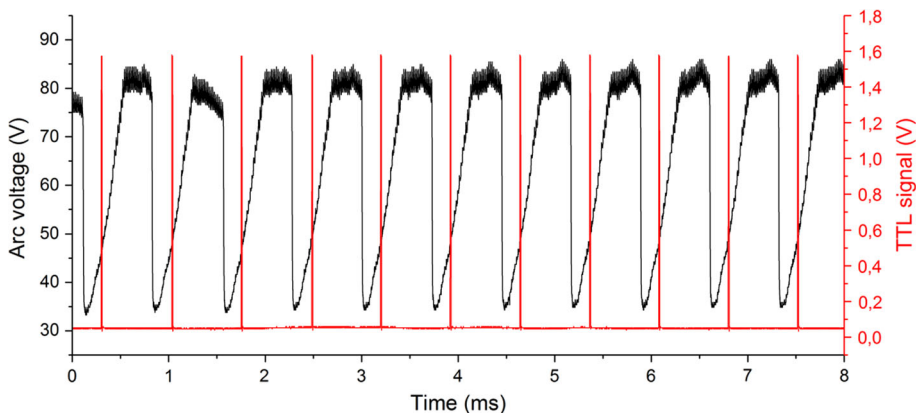


Fig. 5 Voltage signal (black) and TTL signal (red) sent to the printhead by the synchronization device (Color figure online)

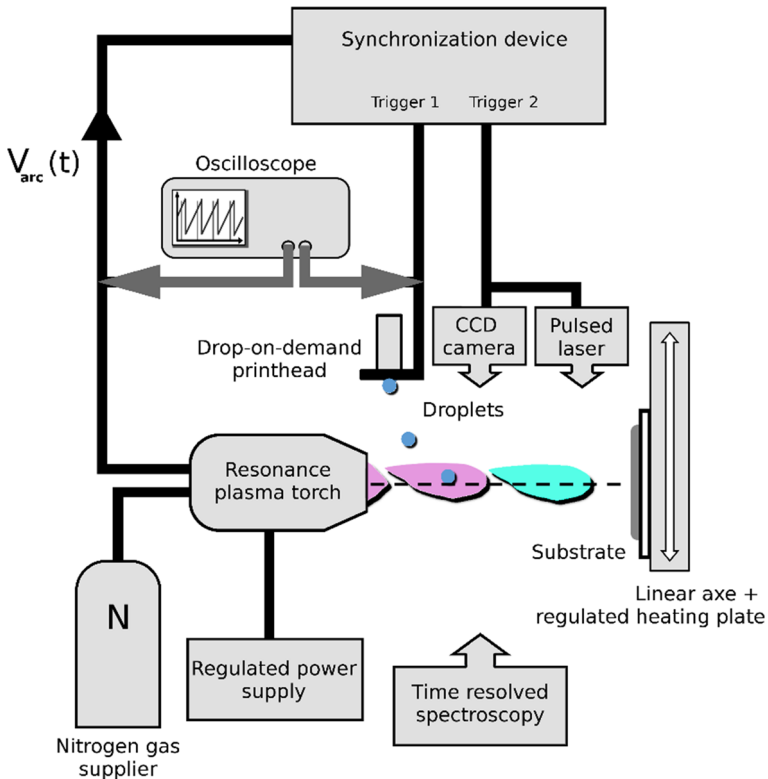


Fig. 6 General schematic view of the experimental setup

Synchronization Setup

The droplets emission was triggered by the arc voltage periodic oscillations. A synchronization device converted the arc voltage signal to a TTL pulse that could be delayed to adjust the injection timing and trigger diagnostics. The signals were monitored with an oscilloscope (Wavesurfer 3024, Teledyne Lecroy, USA), as illustrated in the Fig. 5. A first trigger was sent to the printhead to deliver an individual droplet by deformation of the piezoelectric actuator. A replica of this trigger was also sent to the camera coupled with the pulsed diode laser. A general view of the process is presented in Fig. 6.

Spraying Conditions

The droplet actuation pulse was optimized for stable ejection with an ejection velocity of 3.2 m s^{-1} which corresponds to the maximum velocity obtained with this printhead device. Preliminary studies have shown that the higher the velocity of the droplet, the better it penetrates as close as possible to the axis of the torch, where the temperature is maximum. The spraying distance was optimized according to previous studies at 35 mm [24]. The printhead was fixed at $y = 10 \text{ mm}$ above the axis of the torch and at $z = 5 \text{ mm}$ from the nozzle. To control the temperature and to favor the elaboration of the coatings, the substrates were preheated to $400 \text{ }^\circ\text{C}$ using a regulated heating resistance (Acim Jouanin, France). The speed

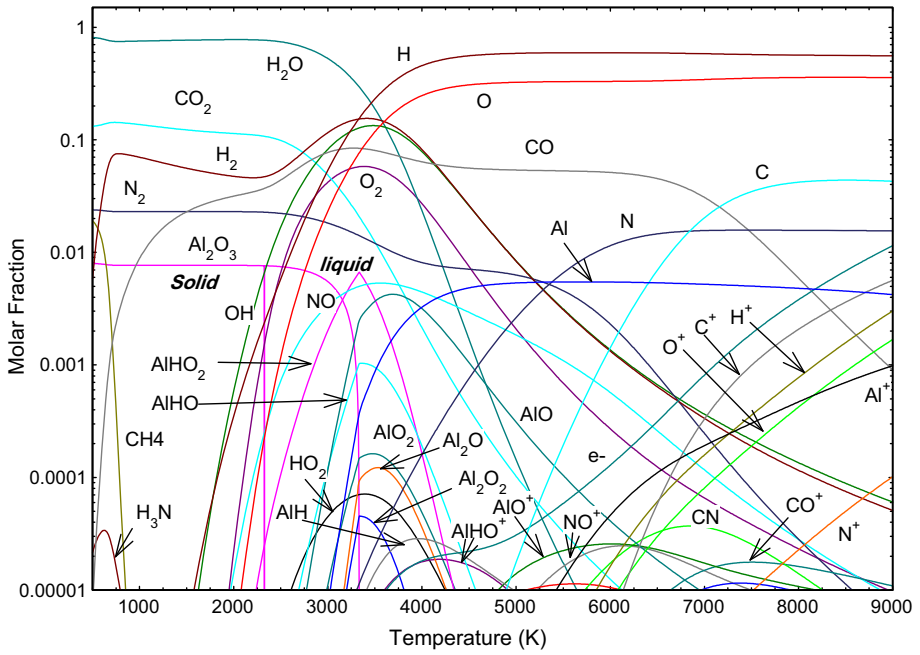


Fig. 7 Molar fraction at chemical equilibrium and at thermal equilibrium calculated at 1 bar and with droplet composition

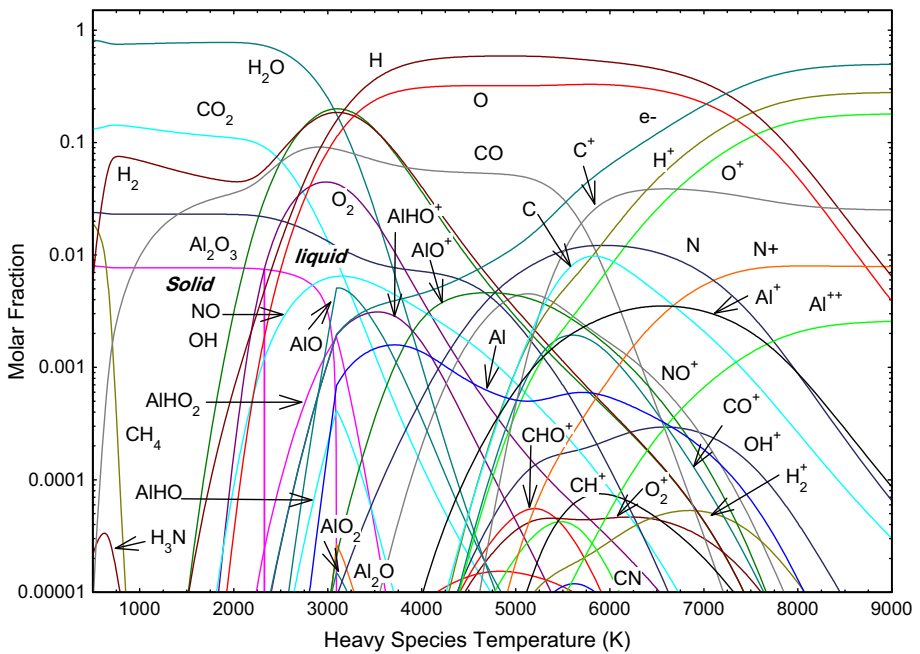


Fig. 8 Molar fraction at chemical equilibrium and out of thermal equilibrium ($\theta = 2$) calculated at 1 bar and with droplet composition

of pass was fixed at 400 mm s^{-1} with an automated linear axis (Robo Cylinder, Rosier Mecatronique, France). The deposition time was set at 10 min, i.e. an effective deposition time of 16 s. The effective deposition time is the real time of material deposition, i.e. the time during which a substrate point receives the plasma jet. The substrates were 1 mm thick mirror-polished stainless steel corresponding to $15 \times 15 \text{ mm}$ squares.

Coatings Characterization

Coating morphology and elemental composition were characterized by Scanning Electronic Microscopy (SEM Quanta, FEI, USA) coupled with an Electron Dispersion Spectrometer (EDS). Imaging and diffraction pattern with Transmission Electronic Microscopy (TEM, JEOL2010, UK) were also used to characterize crystallinity and crystallite sizes. The structural characteristics of the coatings were determined using X-ray diffraction (XRD) with Cu $K\alpha$ radiation (D8 Advance, BRUKER, Germany). The resulting diffractograms were indexed with JCPDS-ICDD database. Interferometer microscopy (Fogale nanotech, France) was used to measure coating thickness.

Results

Calculation of Plasma Chemical Composition

The calculation was made at a pressure of 1 bar at thermal equilibrium (Figs. 7 and 9) and out of thermal equilibrium (Figs. 8 and 10) with an electronic temperature (T_e) twice the heavy species temperature (T_h): $\theta = 2$.

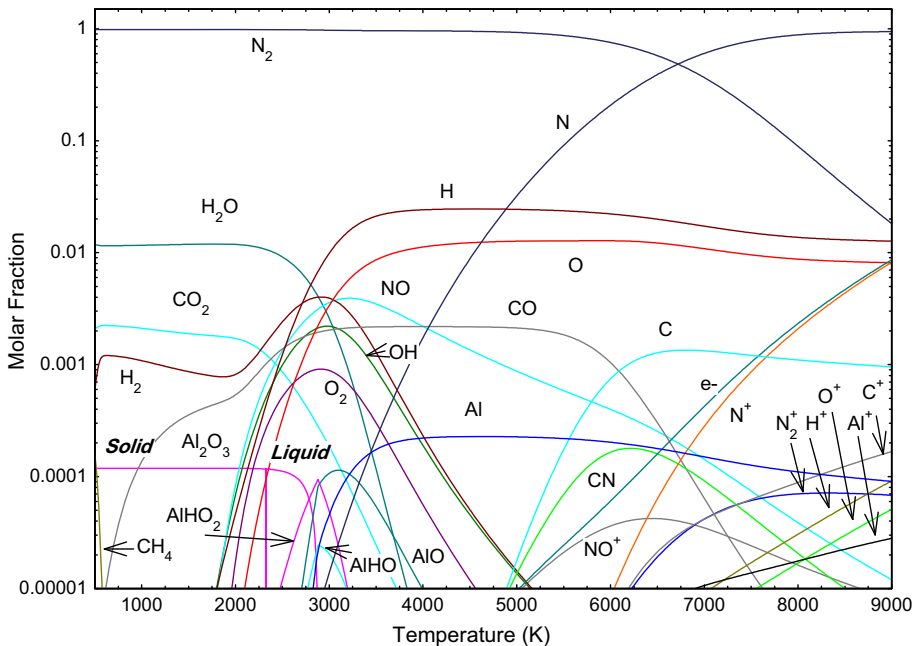


Fig. 9 Molar fraction at chemical equilibrium and at thermal equilibrium calculated at 1 bar and with droplet and nitrogen composition

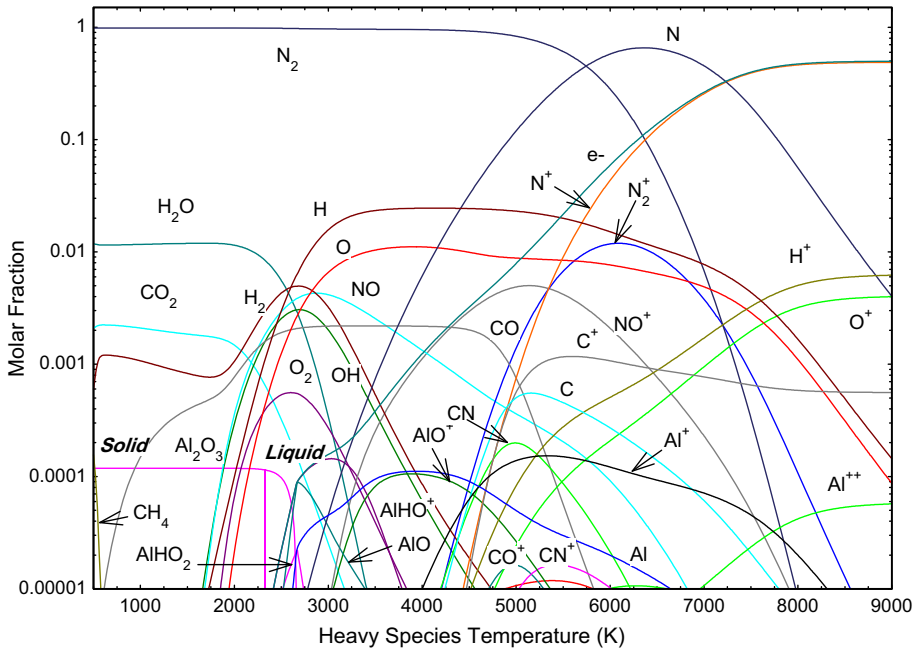


Fig. 10 Molar fraction at chemical equilibrium and out of thermal equilibrium ($\theta = 2$) calculated at 1 bar and with droplet and nitrogen composition

The molar fraction of chemical species versus temperature for the droplet alone was plotted in Figs. 7 and 8. The main condensed phase is the aluminum oxide that is in solid phase below 2327 K and liquid until its vaporization around 3335 K at thermal equilibrium and 3090 K out of thermal equilibrium. The vaporisation of Al_2O_3 liquid produces mainly the diatomic species aluminum monoxide AlO and the polyatomic species AlHO_2 .

The main gaseous species are water vapour H_2O , carbon dioxide CO_2 and nitrogen N_2 . H_2O dissociates in H and O around 3460 K at thermal equilibrium and 3130 K out of thermal equilibrium. CO_2 dissociates in CO and O_2 around 2830 K at thermal equilibrium and 2506 K out of thermal equilibrium. It is interesting to note that at low temperature (below 1500 K), methane and ammonia are formed in minor amounts. Methane is subsequently dissociated into syngas ($\text{H}_2 + \text{CO}$) which explains the steep increase of hydrogen at low temperature.

At thermal equilibrium (Fig. 7), the electrical neutrality is made between electrons and successively mainly with AlHO^+ until around 4865 K, with AlO^+ until a temperature around 5740 K, with Al^+ until a temperature around 6750 K when C is ionized and with C^+ for higher temperature. Out of equilibrium (Fig. 8) the electrical neutrality is made between electrons and successively mainly with AlHO^+ until around 3890 K, with AlO^+ until around 5290 K and with C^+ until around 6400 K and with H^+ for higher temperature.

Concerning the droplet introduced in the nitrogen plasma, the molar fraction of chemical species versus temperature is plotted in Figs. 9 and 10. The main condensed phase is aluminum oxide that is in solid phase below 2327 K and liquid until its vaporization around 2950 K at thermal equilibrium and 2715 K out of thermal equilibrium. The vaporisation of Al_2O_3 produced mainly the diatomic species aluminum monoxide AlO . We do not observe aluminum nitride AlN and Al in condensed phase.

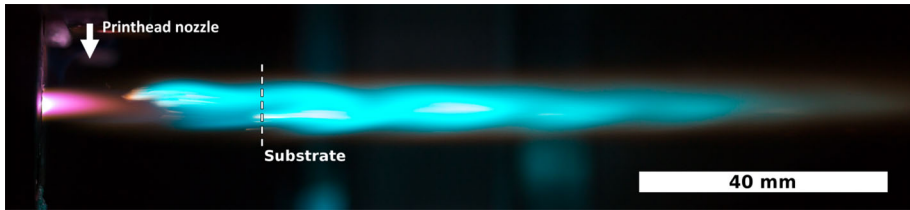


Fig. 11 Synchronous injection of aluminum nitrate in the pulsed arc plasma. Aperture time: 200 μ s

The main gaseous species are nitrogen N_2 , water vapour H_2O and carbon dioxide CO_2 . N_2 start dissociating in N at a temperature higher than considered temperature range, i.e. above 5760 K. Water vapour dissociates at 2790 K at thermal equilibrium and at 2570 K out of thermal equilibrium. CO_2 dissociates in CO and O_2 around 2410 K at thermal equilibrium and 2160 K out of thermal equilibrium. At thermal equilibrium (Fig. 9), the electrical neutrality is made between electrons and NO^+ until around 6400 K and with N^+ for higher temperature. Out of thermal equilibrium (Fig. 10), the electrical neutrality is made between electrons and successively mainly with $AlHO^+$ until around 3400 K, with NO^+ until around 5360 K and with N^+ for higher temperature.

As partial conclusion, the thermodynamic calculations confirm the presence at low temperature of gaseous species possibly leading to combustion, namely CH_4 , H_2 and even NH_3 . Considering the droplet alone, O_2 is formed from the dissociation of CO_2 after the

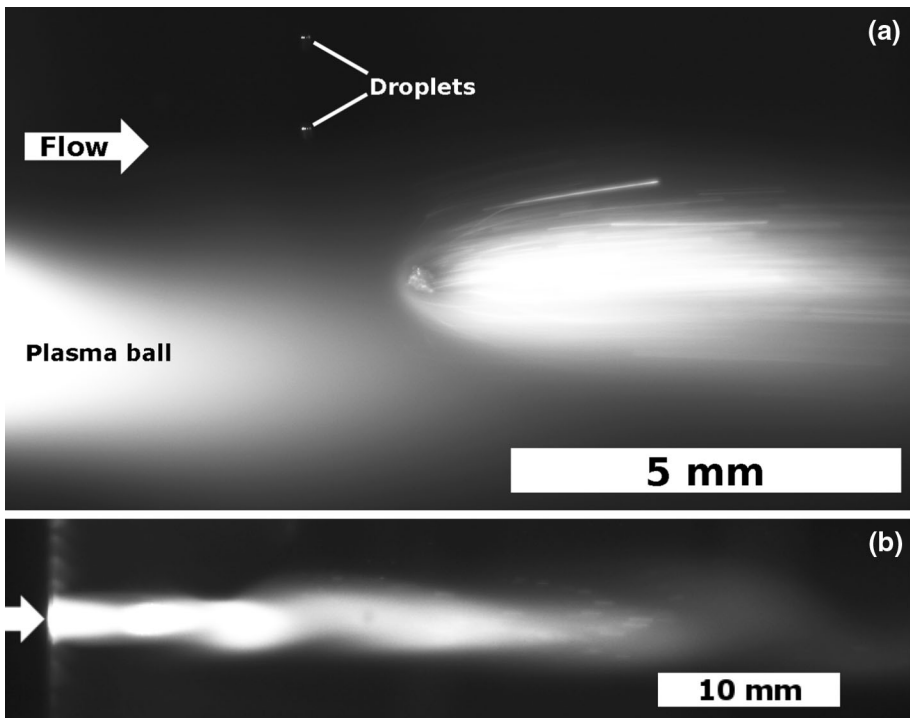


Fig. 12 Synchronous injection of aluminum nitrate in the pulsed arc plasma. Fast shutter camera. Aperture time: 50 μ s. **a** At injection point and **b** at lower magnification

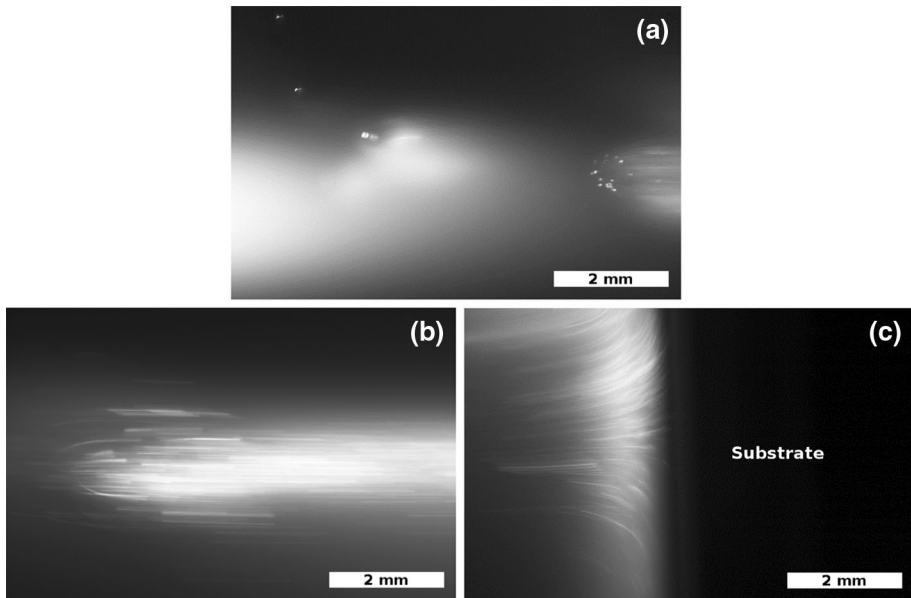


Fig. 13 Imaging of thermal fragmentation of the droplets. Fast shutter camera. Aperture time: 50 μ s. **a** At injection point (camera placed at $z = 5$ mm). **b** In the laminar jet (camera placed at $z = 15$ mm). **c** On substrate (camera placed at $z = 35$ mm)

complete dissociation of combustion gases. This means that combustion does not occur with O_2 resulting from the droplet itself in TGA/DTA but from air atmosphere. Moreover, polyatomic carbonaceous species are either dissociated at low temperature or are negligible.

The initial proportion of nitrogen and droplet plays a key role especially on the vaporization temperature of liquid Al_2O_3 . The concentration of AIO molecule is sensitive to the droplet vaporisation (proportion of liquid vaporized inside the plasma).

The presence of solid alumina is also predicted as hypothesized by TGA/DTA analysis, but the crystallization state is not taken into account. Even with a large amount of nitrogen, AlN and Al in condensed phase do not appear. At last, it was noticed that the composition of the plasma depends on the thermal equilibrium of the plasma notably through the electron concentration.

In-Flight Diagnostics

When injecting aluminum nitrate ink, a blue plasma jet was observed as shown in Fig. 11. This cyan blue color can be attributed to the blue-green system of AIO molecule ($B^2 \sum^+ - X^2 \sum^+$) with the maximum intensity at 484.2 nm (head band for the sequence $\Delta v = v' - v'' = 0$ where v' and v'' are respectively the vibration quantum number of upper and lower transition levels) [34, 35]. At the injection point, the orange color is attributed to the solvent evaporation (water + glycerol). It can be seen that the plasma was widely seeded by the decomposition of the precursor.

The interception of a droplet by a plasma ball is illustrated by means of a synchronous fast shutter camera in Fig. 12. The droplet readily explodes and its vapor spreads over the

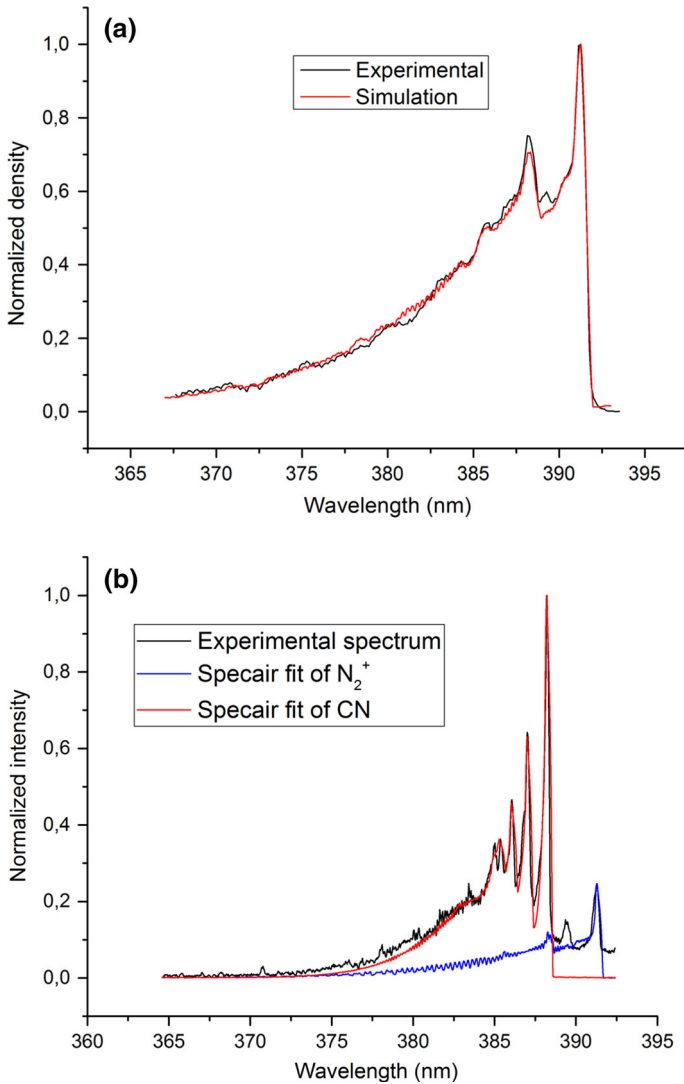


Fig. 14 **a** Specair fit of N₂ spectrum at nozzle exit. **b** Specair fit of CN spectrum at 15 mm

plasma plume. Incandescent streaks are visible from the point of injection throughout the jet, they continue to be distinguished in the plasma jet at greater distances from the nozzle exit for a low magnification (Fig. 12b).

Figure 13 shows time-resolved imaging at different distances z from the nozzle exit. At the injection point (see Fig. 13a) the droplet was caught in the jet and exploded just after penetration. Some droplet fragments seem to have travelled at counter flow as suggested in Figs. 12b and 13b with initial trajectories whose the curved shape originates from the fragmentation point of the droplet.

The particles follow the jet flow (see Fig. 13b). The measurement of incandescent streaks gives an estimate of their speeds, i.e. about 55 m s^{-1} . This value is consistent with plasma velocity at nozzle exit measured in previous study ($\sim 66 \text{ m s}^{-1}$) [22].

When the particles reach the coating at 35 mm (see Fig. 13c), deviations from their axial trajectories are observed.

Supposing these drags come from molten particles of order of $\sim 1 \mu\text{m}$ diameter and with a 1 mm boundary layer, the number of Stokes was estimated to be 0.7. This estimate means that the particles follow the stream of flow which becomes parallel to the substrate and therefore some will not impact [36].

OES diagnostics was used to evaluate the plasma temperature without injection at 1 and 15 mm from the nozzle exit assuming local thermodynamic equilibrium. The first negative system of N_2^+ ($\text{B}^2\Sigma_u^+ - \text{X}^2\Sigma_g^+$) in the 320–400 nm range was measured. At this distance, the obtained N_2^+ spectra do not suffer from strong overlapping with the emission of the violet system of CN molecule ($\text{B}^2\Sigma^+ - \text{X}^2\Sigma^+$) nor the second positive system of N_2 ($\text{C}^3\Pi_u - \text{B}^3\Pi_g$). At 15 mm, the contributions of N_2 and N_2^+ to the spectrum are low, so that at this distance CN emission was used to measure the temperature.

Figure 14 shows the emission spectra of the first negative system of nitrogen $\text{N}_2^+(1-)$ and the violet system of CN in the range 365–395 nm at low spectral resolution. These spectra result from the binning over the height of plasma jet. Although they encompass the contributions of plasma regions with different temperatures, measurements are mainly sensitive to temperatures close to the plasma core.

At nozzle exit, the rotational temperature was measured from the $\Delta v = 0$ vibrational sequence of $\text{N}_2^+(1-)$. Simulations were carried out with Specair with a trapezoid slit function of base 0.1 nm and top 1.1 nm. The rotational temperature thus obtained was equal to $7075 \pm 200 \text{ K}$ at 1 mm from the nozzle exit. Further downstream from the exit, the emission of $\text{N}_2^+(1-)$ decreased and the measurement of temperature from this system was no more possible. However, at 15 mm, the molecular spectrum of CN was used to measure the rotational temperature. As shown in Fig. 14b, the contribution of N_2^+ to this

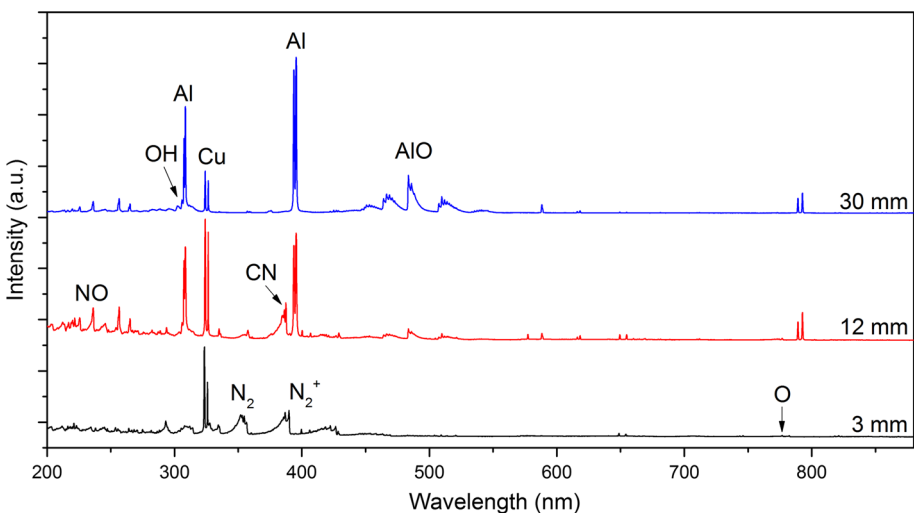


Fig. 15 OES spectrum of a synchronous solution injection into the pulsed arc plasma, at different distances

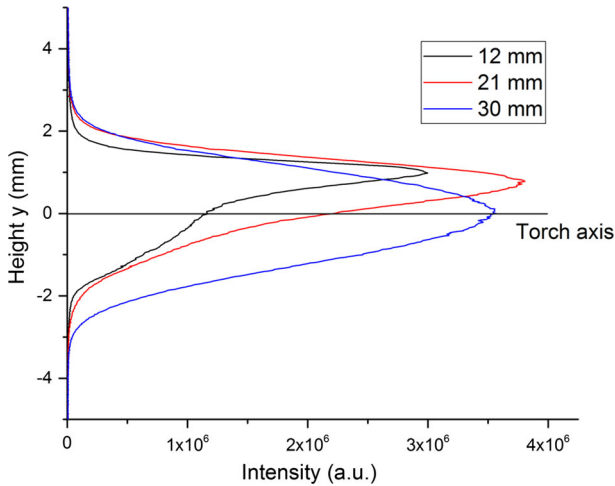


Fig. 16 Emission profile of AIO ($B^2\Sigma^+ - X^2\Sigma^+$) at 464.8 nm for different distances from the nozzle

spectrum is weak and its influence on the spectrum fit as well. At 15 mm, the best spectrum fit finally gives an approximate temperature of 5400 K.

Figure 15 shows the emission spectrum of the plasma with injection at different distances from the nozzle exit. At 3 mm, before the injection point, the spectrum was essentially composed of the first negative system N_2^+ and the second positive system of N_2 emission between 300 and 450 nm. A weak contribution of CN is also noticed around 387 nm coming from the carbon dioxide from the surrounding atmosphere. The molecule OH is observed (~ 308 nm for $A^2\Sigma^+ - X^2\Pi$ transition) which indicates the presence of water at 12 mm from the nozzle exit. The source of this water could be the decomposition of the injected solution as shown by the calculation of plasma composition and steam from ambient air. The emission lines detected around 325 nm are attributed to atomic copper

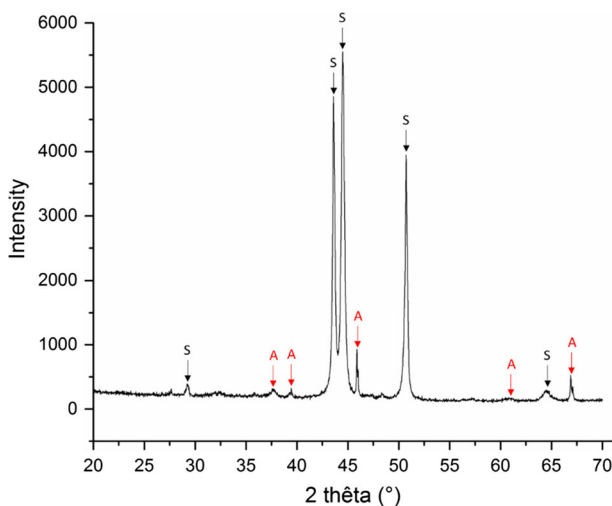


Fig. 17 XRD spectra of coating. S: substrate indexation, A: γ -alumina indexation

lines resulting from the anode erosion due to arc attachment. After the injection point, droplets are thermally decomposed by the plasma jet and atomic aluminum exhibits strong emission. Its intensity increases with distance. Such a metallic vapor is readily excited due to low excitation energies, 2.8 eV at 394.4 nm and 3.6 eV at 308.2 nm. The same observation can be made for the molecular emission of AlO, formed just after the injection point, which increases progressively with the distance. Note that the excitation energy of AlO electronic state ($B^2\Sigma^+$) is only about 2.6 eV [35]. At last, it is observed that excited oxygen atoms shows a reduction in their emission at higher distances due to cooling of the plasma and relatively higher excitation energy (~ 10 eV at 777.5 nm) than AlO and Al (I).

The emission of excited oxygen atoms is relatively independent of the liquid injection showing that oxygen coming from droplet decomposition weakly contributes to the emission.

Figure 16 describes the emission profile of AlO ($B^2\Sigma^+ - X^2\Sigma^+$) at different distances from the nozzle. Near the injection point, at 12 mm, the emission is concentrated in the fringes of the plasma jet. This is represented by a peak of emission shifted from the axis of the torch. Further downstream, this peak gets closer to the axis. This means that the reaction is spreading inside the jet. At 30 mm, the reaction reaches the heart of the jet. The peak of emission is centered with the torch axis. At this distance, the plasma jet is homogenous.

Coatings

In line with the OES results, EDS analysis confirmed the presence of oxygen and aluminum only, with an aluminum/oxygen ratio of 2–3. There is no nitrogen. This confirms the predominance of the oxidation reactions of aluminum.

XRD indexation (Fig. 17) showed only the γ -Al₂O₃ crystalline phase (JCPDS No. 01-074-2206).

Coating surface is nanostructured into cauliflowers shapes from a few micrometers, composed by nanometric grains, as seen in Fig. 18. The structures look very porous, this was confirmed by the high specific surface area of 125.2 m² g⁻¹ measured by BET method (ASAP 2020, Micromeritics, USA).

The TEM characterization showed that the cauliflowers structures were composed only of amorphous grains relatively uniform in size around 10 nm (Fig. 19a, c). Spherical

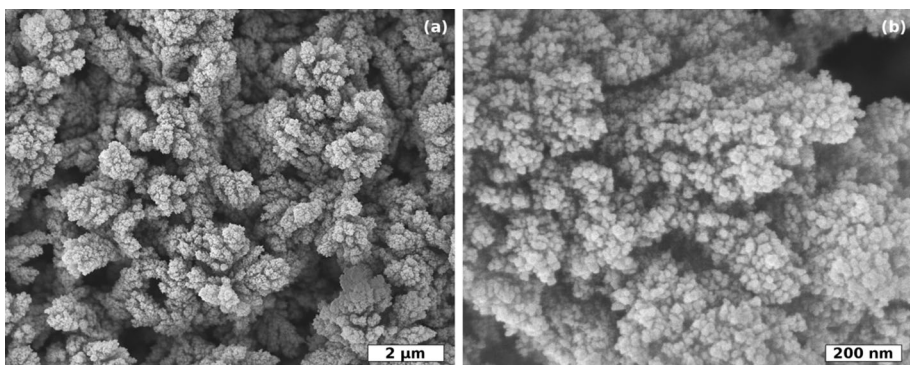


Fig. 18 SEM pictures of coating top surface. **a** Magnification $\times 10,000$ and **b** $\times 100,000$

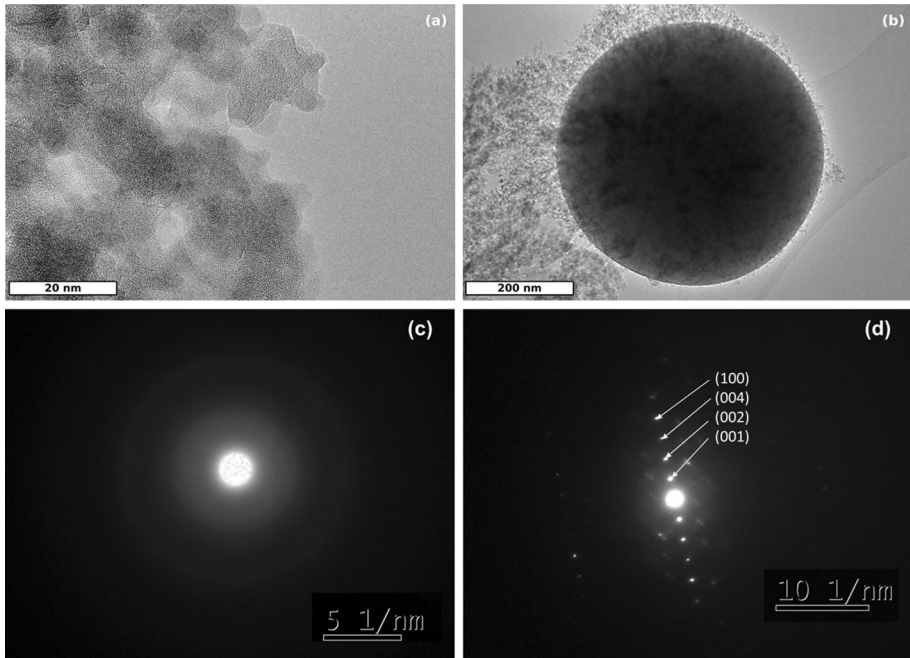


Fig. 19 TEM image of coating. Magnification **a** $\times 300,000$ and **b** $\times 30,000$. Diffraction patterns of cauliflowers grains (**c**) and spherical particles (**d**) indexed with γ -alumina (JCPDS database: 04-016-7505)

particles were also observed as inclusions in cauliflowers. The particles correspond to crystallized γ -alumina micro-sized spheres (Fig. 19b, d).

Discussion

The main challenge in plasma spraying of liquid feedstock is to control the trajectories of products resulting from the fragmentation processes of droplets. In highly fluctuating plasma jet associated with a continuous injection of liquids, large dispersion of trajectories with heterogeneous plasma treatment is expected. By the use of pulsed liquid injection, the adjustment of the injection timing with respect to plasma oscillation enables the momentum density of liquid to be tuned to match that of the plasma jet. The synchronous injection of droplets has been shown to efficiently reduce this dispersion and to give rise to more homogeneous coatings [23]. A mass deposition efficiency of 74% was obtained for the coatings with synchronized injection against 55% for deposits without synchronization (the injection was triggered at 1.4 kHz without the synchronization device). The characteristic time of acceleration of one droplet immersed within the plasma is given by $\tau_{\text{acc}} = \rho_l d^2 / 18\eta$ where ρ_l , d and η are respectively liquid density, droplet diameter and plasma viscosity. Considering the plasma data at mean enthalpy 17 MJ kg^{-1} (see Sect. 2.1) given by [37], the acceleration time is about 2.3 ms which is longer than the plasma period of 0.7 ms. Droplet acceleration is weak and, without fragmentation, droplets would not follow the modulation of plasma velocity highlighted in previous study [22].

The Weber number, $We = \rho_p v_p^2 d / \sigma_\ell$ where ρ_p , v_p and σ_ℓ are respectively the density and speed of plasma, and the liquid surface tension, was estimated < 1 . This low value seems to rule out mechanical fragmentation. Low plasma velocity prevents mechanical fragmentation which is undesirable because it leads to the division of the main droplet into smaller droplets with uncontrolled trajectories [38]. Instead fragmentation processes governed by heat transfer are likely to occur as shown in Figs. 12 and 13. The solvent vaporization time was estimated to be about 0.1 ms by the following equation [23]:

$$\tau_{\text{vap}} = \frac{\rho_\ell L_v}{4Nu a_\phi} \left(\frac{d^2}{h_p} \right) \left[1 - \left(\frac{d_s}{d} \right)^2 \right] \tag{2}$$

where L_v the latent heat of vaporization (kJ kg^{-1}), Nu the Nusselt number, a_ϕ the coefficient of heat potential [39], h_p the mean plasma specific enthalpy, d_s the diameter of the solid phase after evaporation.

The vaporization time is smaller than the plasma period and the acceleration time. This is qualitatively confirmed by observations in Figs. 12 and 13 where thermal fragmentation occurred before any acceleration in the first millimeters after the injection point. Moreover, if we consider that, at the end of vaporization (τ_{vap}), liquid is replaced by vapor, the vaporization speed u_{vap} , approximated by $u_{\text{vap}} = \frac{d}{2\tau_{\text{vap}}} \left(\frac{\rho_\ell}{\rho_{\text{vap}}} \right)^{1/3}$ where ρ_{vap} is the vapor density, is about 5 m s^{-1} . This gives the radial speed at which the sphere that contains the vapor inflates [23]. It also suggests the possibility of a centrifugal fragmentation process, thermally induced, where some fragments are traveling at counter flow before being trapped by the flow and participate to the seeding of plasma balls as seen in Figs. 12 and 13.

TGA/DTA measurements suggested possible combustion reactions that could have governed the droplet vaporization. It must be emphasized that combustion can only occur from O_2 due to air mixing with the plasma as shown in Sect. 3.1. It was observed in Fig. 15 that the intensities of oxygen atomic lines (O triplet at 777 nm) were weak and did not depend on the liquid injection. Moreover, air mixing is expected to be smoother than in the case of higher powered plasma torches where air engulfment with eddies was previously reported [14]. This is because the plasma jet is laminar and slow cooling with oxygen diffusion from the jet fringes can be supposed. The temperatures of the plasma core at about 15 and 35 mm from the nozzle exit (location of substrate) were estimated to be close to respectively 5400 K and 4000–4500 K by monitoring the emission of OH molecular bands (A–X system). The latter was related to H_2O of solution precursor and more weakly linked to the presence of steam in air. The calculation of the binary diffusion coefficient D_{ij} of O_2 into N_2 shows that D_{ij} varies between 0.6×10^{-4} and $2 \times 10^{-3} \text{ m}^2 \text{ s}^{-1}$ for temperatures ranging between 2000 and 4000 K (before O_2 dissociation). The characteristic time of oxygen diffusion is roughly $\tau_D = \delta^2 / D_{ij}$, where δ is a characteristic length of diffusion ($\sim 1 \text{ mm}$). Then, $\tau_D \approx 0.8 \text{ ms}$ at 3500 K for $D_{ij} = 1.2 \times 10^{-3} \text{ m}^2 \text{ s}^{-1}$. Moreover, the time of flight of vapors to reach the substrate is approximately 0.5 ms if they have the plasma velocity. This evaluation shows that oxygen diffusion from the fringes exists but is not efficient.

At last, evidences of carbon presence were not found (neither C2 Sawn band emission nor solid carbon in coatings). However, combustion cannot be completely discarded at the very early stages of plasma/droplet interaction (i.e. vaporization during the first 100 μs) despite the plasma heating rate is very different from that of TGA/DTA.

Fragmentation generates some vapors resulting from the precursor solution decomposition but also some incandescent materials. The latter were collected at about 15 mm from the nozzle exit on a carbon adhesive. This revealed micro-sized solid particles containing aluminum and oxygen elements by means of SEM and EDS analysis. According to TGA/DTA measurements, aluminum oxides are produced due to thermal decomposition of the initial ink. Thermodynamic calculations confirm this assumption and preferentially predict the formation of alumina instead of aluminum nitride. Below 1000 °C, TGA/DTA analysis does not evidence crystallization which therefore likely occurs in-flight at higher temperatures as suggested by TEM measurements.

Spectroscopic measurements highlighted the presence of aluminum metallic vapor and AIO molecules as also anticipated by theoretical calculation of plasma composition. Calculations showed that the formation of AIO molecules at low temperature resulted from

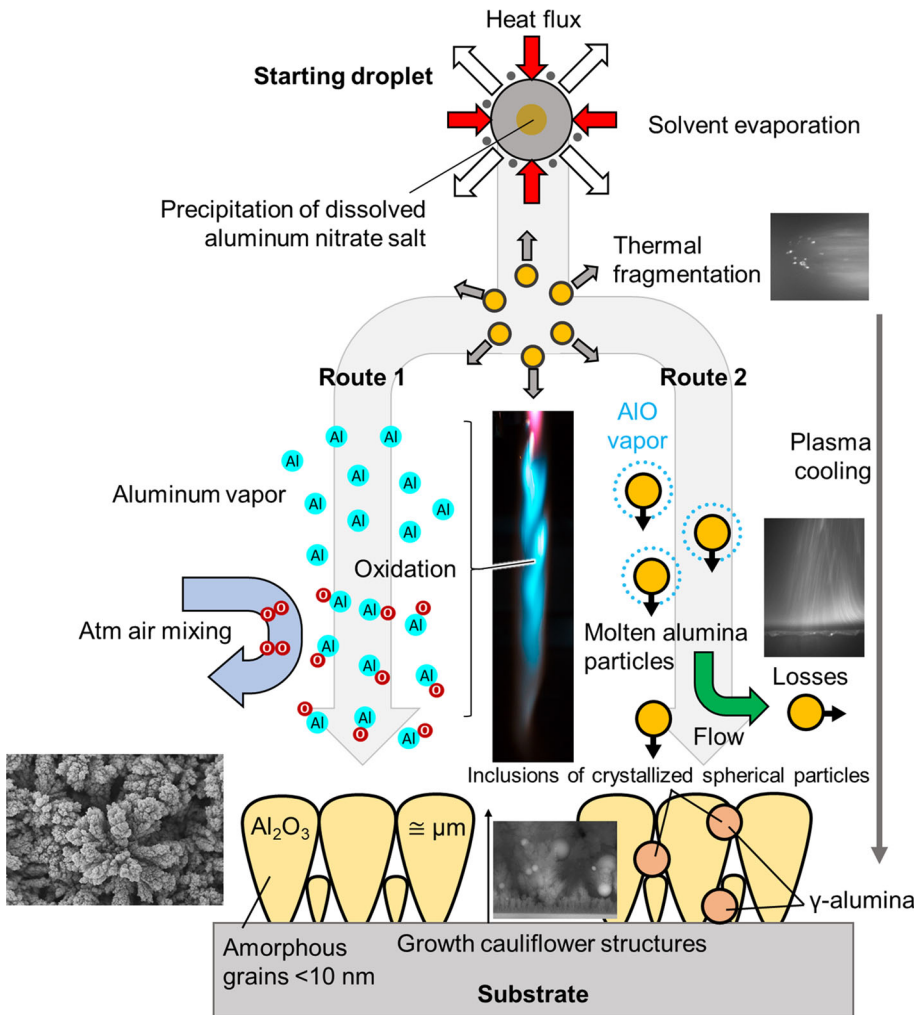


Fig. 20 Kinetic pattern of interactions between plasma and injected material

the vaporization of liquid alumina. At higher temperatures, chemical reactions between gas species must be considered, such as the oxidation of aluminum to form aluminum monoxide.

Calculations also showed that the vaporization temperature of liquid alumina was decreased when using nitrogen as plasma forming gas. This promotes the coating formation from vapors condensation. Non-thermal equilibrium also affects the vaporization temperature by displacing the chemical equilibrium.

The characterization of coatings shows cauliflower structures of alumina with amorphous grains. They have weak adhesion on mirror-polished and pre-heated substrates. These typical microstructures suggest a mechanism of vapor condensation on the substrate. Despite a substrate temperature imposed (400 °C), vapor condensation may occur at too low temperature, which does not allow crystallization of these grains. Inclusions of crystalline spherical particles are observed in amorphous microstructures. These particles are not deformed into splats, probably because of low plasma velocity. It is worth mentioning that amorphous alumina coatings may have interesting properties, for example for anti-corrosion barriers at ambient temperature [40].

The study of ink thermal decomposition, the use of thermodynamic calculations, the characterization of plasma properties and the analysis of deposited materials validate the assumption that aluminum oxides are preferentially formed instead of aluminum nitride contrarily to what stated in [23, 24].

One envisaged perspective would be to modify the reaction path improving the nitriding reaction. Shahien et al. [41] proposed adding ammonium chloride NH_4Cl to make AlN with an aluminum powder by a chlorination-nitridation sequences.

Figure 20 summarizes the in-flight mechanisms described above from the ink decomposition leading to two simultaneous routes. The first one depicts the formation of coatings from the oxidation of the vapor phase. The second route focuses on the formation of aluminum oxides, which are consolidated in-flight at high temperature, melted by the plasma and produce crystallized inclusions inside the coating.

Conclusion

A low powered plasma torch was used to deposit ceramic coatings. This custom made torch operates in pulsed mode with regular oscillations obtain by adjusting torch dimensions and by using a modulated arc current.

An inkjet drop-on-demand printhead is used to deliver the liquid material of solution precursors. The droplet is triggered by the plasma torch itself to inject in each plasma oscillation the material with the same operational parameters in order to isolate and control the plasma/droplet interaction.

An aluminum nitrate ink was formulated in order to observe the aluminum reactions from the injection point to the substrate.

The mains results of this original process are:

- Atmospheric nitrogen plasma in this range of temperature and this aluminum nitrate salt concentration led to the deposit of an aluminum oxide coating. The use of nitrate and nitrogen plasma did not produce nitrides.
- The droplet exploded due to thermal fragmentation producing vapors and micro-sized particles in the plasma jet.

- The synchronization allowed a homogeneous treatment which isolated two routes of coating formation: cauliflowers condensation on substrate and spherical particles.
- The deposit of the material led to amorphous nanostructured cauliflowers shapes of a few micrometers with a high specific surface area.
- The inclusion of micrometric crystallized spherical particles was observed. Their low Stokes number tends to show that they were partly deviated from the substrate.
- In a previous study, very close experimental conditions with a nano-suspension of titanium dioxide made it possible to obtain similar nanostructured coatings but with crystallized TiO₂ materials [23]. An SPS/SPPS comparison with an alumina suspension could be considered.

This work has allowed better understanding of in-flight mechanisms in SPPS process. Further investigations will be necessary to optimize coatings, e.g. the substrate adhesion, the nitridation mechanism and the crystallization of the nano-grains.

Acknowledgements We are grateful to the Electric Arc Association (AAE) for their financial support (0C2AA043Z). We thank Limoges University materials characterization platform CARMALIM for their assistance. Sébastien Faure, Nicolas Lory and Geoffroy Rivaud are thanked for technical assistance in the experimental setup.

References

1. Thermal Spray Coatings Market by Material (Ceramic, Metals & Alloys), Process (Combustion Flame, Electrical Energy), End-Use Industry (Aerospace, Automotive, Healthcare, Energy & Power, Electronics), and Region—Global Forecast to 2021. <http://www.marketsandmarkets.com/Market-Reports/thermal-spray-coating-market-181347083.html>. Accessed Oct 2017
2. Sampath S (2015) Thermal spray applications in electronics and sensors: past, present, and future. *J Therm Spray Technol*. <https://doi.org/10.1007/s11666-010-9475-2>
3. Fauchais P (2015) Current status and future directions of thermal spray coatings and techniques, Chap.2. In: Espallargas N (ed) *Future development of thermal spray coatings*, 1st edn. Woodhead Publishing. <https://www.elsevier.com/books/future-development-of-thermal-spray-coatings/espallargas/978-0-85709-769-9>
4. Boer J, Burckhardt W (1997) Nanosize powders prepared by flame pyrolysis, *Key Engineering Materials*. *Trans Tech Publ* 132:153–156. <https://doi.org/10.4028/www.scientific.net/KEM.132-136.153>
5. Karthikeyan J, Berndt CC, Tikkanen J, Wang JY, King AH, Herman H (1997) Nanomaterial powders and deposits prepared by flame spray processing of liquid precursors. *Nanostruct Mater* 8(1):61–74. [https://doi.org/10.1016/S0965-9773\(97\)00066-4](https://doi.org/10.1016/S0965-9773(97)00066-4)
6. Killinger A, Gadow R, Mauer G, Guignard A, Vaßen R, Stöver Detlev (2011) Review of new developments in suspension and solution precursor thermal spray processes. *J Therm Spray Technol* 20(4):677–695. <https://doi.org/10.1007/s11666-011-9639-8>
7. Bertolissi G, Chazelas C, Bolelli G, Lusvarghi L, Vardelle M, Vardelle A (2012) Engineering the microstructure of solution precursor plasma-sprayed coatings. *J Therm Spray Technol* 21(6):1148–1162. <https://doi.org/10.1007/s11666-012-9789-3>
8. Shivakumar G, Ramakrishna M, Dusane RO, Joshi SV (2015) Effect of SPPS Process parameters on in-flight particle generation and splat formation to achieve pure α -Al₂O₃ coatings. *J Therm Spray Technol* 24(7):1221–1234. <https://doi.org/10.1007/s11666-015-0284-5>
9. Jordan E, Jiang C, Gell M (2015) The solution precursor plasma spray (SPPS) process: a review with energy considerations. *J Therm Spray Technol* 24(7):1153–1165. <https://doi.org/10.1007/s11666-015-0272-9>
10. Candidato R, Sokołowski P, Pawłowski L, Lecomte-Nanaa G, Constantinescu C, Denoirjean A (2017) Development of hydroxyapatite coatings by solution precursor plasma spray process and their microstructural characterization. *Surf Coat Technol* 318:39–49. <https://doi.org/10.1016/j.surfcoat.2016.10.072>

11. Fauchais P, Vardelle M, Goutier S, Vardelle A (2015) Key challenges and opportunities in suspension and solution plasma spraying. *Plasma Chem Plasma Process* 35:511–525. <https://doi.org/10.1007/s11090-014-9594-5>
12. Rat V, Mavier F, Coudert JF (2017) Electric arc fluctuations in DC plasma spray torch. *Plasma Chem Plasma Process* 37(3):549–580. <https://doi.org/10.1007/s11090-017-9797-7>
13. Etchart-Salas R, Rat V, Coudert JF, Fauchais P, Caron N, Wittman K, Alexandre S (2007) Influence of plasma instabilities in ceramic suspension plasma spraying. *J Therm Spray Technol* 16(5):857–865. <https://doi.org/10.1007/s11666-007-9084-x>
14. Pfender E, Fincke J, Spores R (1991) Entrainment of cold gas into thermal plasma jets. *Plasma Chem Plasma Process* 11(4):529–543. <https://doi.org/10.1007/BF01447164>
15. Heimann RB (2008) Plasma spray coating principles and applications, 2nd edn. Wiley-VCH, New York
16. Pan W, Zhang W, Zhang W, Wu C (2001) Generation of long, laminar plasma jets at atmospheric pressure and effects of flow turbulence. *Plasma Chem Plasma Process* 21(1):23–35. <https://doi.org/10.1023/A:1007037327834>
17. Meillot E, Vincent S, Caruyer C, Damiani D, Caltagirone JP (2013) Modelling the interactions between a thermal plasma flow and a continuous liquid jet in a suspension spraying process. *J Phys D Appl Phys*. <https://doi.org/10.1088/0022-3727/46/22/224017>
18. Fauchais PL, Heberlein JVR, Boulos MI (2014) Thermal spray fundamentals—from power to part. Springer, Berlin
19. Krowka J, Rat V, Coudert JF (2013) Resonant mode for a dc plasma spray torch by means of pressure–voltage coupling: application to synchronized liquid injection. *J Phys D Appl Phys* 46:224018
20. Krowka J, Rat V, Goutier S, Coudert JF (2014) Suspension phased injection in pulsed arc jet for coating elaboration. *J Therm Spray Technol* 23:786–794. <https://doi.org/10.1007/s11666-014-0081-6>
21. Rat V, Krowka J, Coudert JF (2015) Modulation of the specific enthalpy of a pulsed arc plasma jet. *Plasma Sources Sci Technol* 24:045009
22. Rat V, Coudert JF (2016) Theoretical and experimental investigations of the coupling of time-dependent parameters in a blown arc plasma torch. *J Phys D Appl Phys* 49:065203
23. Mavier F, Rat V, Bienia M, Lejeune M, Coudert JF (2017) Suspension and precursor plasma spraying by means of synchronous injection in a pulsed arc plasma. *Surf Coat Technol* 318:18–27. <https://doi.org/10.1016/j.surfcoat.2016.08.061>
24. Mavier F, Lemesre L, Rat V, Bienia M, Lejeune M, Coudert JF (2017) Pulsed arc plasma jet synchronized with drop-on-demand dispenser. *J Phys Conf Ser*. <https://doi.org/10.1088/1742-6596/825/1/012009>
25. Mavier F, Rat V, Coudert JF (2017) Influence of time-modulation of applied current on arc stability in DC pulsed plasma spray torch. *IEEE Trans Plasma Sci* 45(4):565–573. <https://doi.org/10.1109/TPS.2016.2631894>
26. Pacewska B, Keshr M (2002) Thermal transformation of aluminium nitrate hydrate. *Thermochim Acta* 385:73–80. [https://doi.org/10.1016/S0040-6031\(01\)00703-1](https://doi.org/10.1016/S0040-6031(01)00703-1)
27. Melnikov P, Nascimento VA, Arkhangelsky IV, Zaroni Consolo LZ, de Oliveira LCS (2013) Thermolysis mechanism of chromium nitrate nonahydrate and computerized modeling of intermediate products. *J Therm Anal Calorim* 114(3):1021–1027. <https://doi.org/10.1007/s10973-013-3106-3>
28. Fromm J (1984) Numerical calculation of the fluid dynamics of drop-on-demand jets. *IBM J Res Dev* 28:322–333
29. Dou B, Dupont V, Williams PT, Chen H, Ding Y (2009) Thermogravimetric kinetics of crude glycerol. *Biores Technol* 100:2613–2620. <https://doi.org/10.1016/j.biortech.2008.11.037>
30. Zhang M, Xue W, Su B, Bao Z, Wen G, Xing H (2017) Conversion of glycerol into syngas by rotating DC arc plasma. *Energy* 123:1–8. <https://doi.org/10.1016/j.energy.2017.01.128>
31. André P, Abbaoui M, Augéard A, Desprez P, Singo T (2016) Study of condensed phases, of vaporization temperatures of aluminum oxide and aluminum, of sublimation temperature of aluminum nitride and composition in an air aluminum plasma. *Plasma Chem Plasma Process* 36(4):1161–1175. <https://doi.org/10.1007/s11090-016-9704-7>
32. De Vos JC (1954) A new determination of the emissivity of tungsten ribbon. *Physica* 20:690–714
33. Laux CO, Gessman RJ, Kruger CH, Roux F, Michaud F, Davis SP (2001) Rotational temperature measurements in air and nitrogen plasmas using the first negative system of N^{2+} . *J Quant Spectrosc Radiat Transfer* 68(4):473–482. [https://doi.org/10.1016/S0022-4073\(00\)00083-2](https://doi.org/10.1016/S0022-4073(00)00083-2)
34. Pearse RWB, Gaydon AG (1976) The identification of molecular spectra, 4th edn. Chapman and Hall, New-York
35. Saksena MD, Deo MN, Sunanda K, Behere SH, Londhe CT (2008) Fourier transform spectral study $B^2\Sigma^+ - X^2\Sigma^+$ system of AlO. *J Mol Spectrosc* 247:47–56. <https://doi.org/10.1016/j.jms.2007.10.002>

36. Fauchais P, Vardelle M, Vardelle A, Goutier S (2015) What do we know, what are the current limitations of suspension plasma. *J Therm Spray Technol* 24(7):1120–1129. <https://doi.org/10.1007/s11666-015-0286-3>
37. Boulos MI, Fauchais P, Pfender E (1994) *Thermal plasmas: fundamentals and applications*, vol 1. Plenum Publishing Co, New York
38. Fauchais P, Vardelle A (2011) Innovative and emerging processes in plasma spraying: from micro- to nano-structured coatings. *J Phys D Appl Phys*. <https://doi.org/10.1088/0022-3727/44/19/194011>
39. Rat V, Coudert JF (2006) A simplified analytical model for dc plasma spray torch: influence of gas properties and experimental conditions. *J Phys D Appl Phys* 39:4799–4807. <https://doi.org/10.1088/0022-3727/39/22/010>
40. Samélor D (2011) Amorphous alumina coatings: processing, structure and remarkable barrier properties. *J Nanosci Nanotechnol* 11:1–5
41. Shahien M, Yamada M, Yasui T, Fukumoto M (2011) Influence of NH_4Cl powder addition for fabrication of aluminum nitride coating in reactive atmospheric plasma spray process. *J Therm Spray Technol* 20:205–212. <https://doi.org/10.1007/s11666-010-9584-y>